Essential refinements of spherical nanoindentation protocols for the reliable determination of mechanical flow curves

A. Leitner [a], V. Maier-Kiener [b], D. Kiener [a,*]

[a] Department Materials Physics, Montanuniversität Leoben, Jahnstraße 12, A-8700 Leoben, Austria
[b] Department Physical Metallurgy and Materials Testing, Montanuniversität Leoben, Roseggerstraße 12, A-8700 Leoben, Austria

HIGHLIGHTS

- Novel calibration procedure for spherical tips based on fundamental geometrical considerations
- Implementation of strain-rate controlled tests enhances utility of spherical nanoindentation test
- Successful determination of strain-rate sensitivity by multiple constant strain-rate tests and strain-rate jump tests
- Experimental determination of the constraint factor and introduction of a method to continuously obtain C^* during testing
- Extracted nanoindentation flow curve are in excellent agreement with comparative micropillar tests on the identical samples

GRAPHICAL ABSTRACT
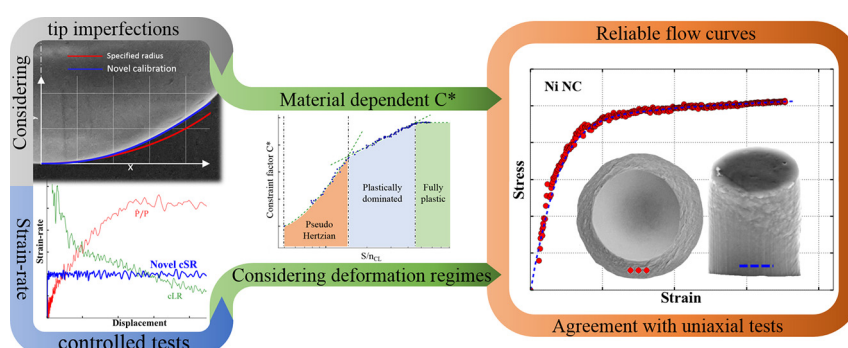
ARTICLE INFO

ABSTRACT

Understanding and linking mechanical properties obtained by spherical indentation experiments to uniaxial data is extremely challenging. Since the first attempts in the early 20th century numerous advances gradually allowed to expand the output of indentation tests. Still, the extraction of flow curves from spherical nanoindentation has not yet been fully established, as tip shape problems and size effects impede a straight-forward implementation. Within this study, we show new calibration procedures originating from fundamental geometrical considerations to account for tip shape imperfections. This sets the base for strain-rate controlled tests, which in turn enables us to measure rate-dependent material properties either with constant strain-rate or by strain-rate jump tests. Finally, experimental evaluation of the constraint factor in consideration of the mechanical properties and induced strain enables the extraction of flow curves. Testing materials with refined microstructures ensures the absence of possible size-effects. This study contributes to a significant improvement of current experimental protocols and allows to move flow curve measurements from single spherical imprints one step closer to its implementation as a standard characterization technique for modern materials.

1. Introduction

Fast, comprehensive and reliable mechanical characterization of materials gains significance to keep pace with the rapid developments in engineering and material science disciplines. However, contrary to

* Corresponding author.
E-mail addresses: alexander.leitner@unileoben.ac.at (A. Leitner), verena.maier-kiener@unileoben.ac.at (V. Maier-Kiener), daniel.kiener@unileoben.ac.at (D. Kiener).

conventional materials, modern high-performance components, micro-electronics or functional materials are often produced at a laboratory bench scale or by bottom-up techniques which must cope with local variations of mechanical properties. These structures owe their strength and functionality to specific local micro- and nanoscale features. Fundamentally understanding such materials often requires highly localized measurements, which are also important once higher-level simulation techniques are involved that necessitate stress-strain curves as an input. Hence, a micromechanical technique is required to comply with the needs of minimal material consumption, high local sensitivity and cost-effectiveness but at the same time maximum exploitation of data while maintaining high reliabilities.

Instrumented indentation with its long history [1–6] is well established nowadays and one of the most promising candidates to meet these requirements. Besides, it is available in almost any modern material research lab, main assets are straight-forward sample preparation and highly automated procedures. Therefore, nanoindentation has become a standard technique to measure the hardness H and the Young's modulus E of materials [2,7]. Since dynamic indentation setups became available, elastic and plastic properties can continuously be recorded over displacement [2,8–11] and allow to assess the reliability of tests on isotropic samples or to account for thermal drift influences during long term-tests [12]. Highly hydrostatic stress fields emerge underneath the indenter tip [13] and consequently also enable characterization of brittle materials at high strains.

The flip side of nanoindentation is mainly the occurrence of length scale effects such as geometry dependent indentation size effects which complicate the analysis [14–18]. Also, the fabrication of precise tip shapes is a challenging task. Considering that indentation tips should be extremely hard and stiff only a few ceramic materials can be used. Finally, in terms of flow curve extraction the complex multi-axial stress and strain field imposed by indentation [13,19,20] impedes a straight-forward analysis.

Revealing the flow behavior of materials can principally be attempted in two different ways. On the one hand, various self-similar indenter tips, such as pyramids or cones, with varying opening angle can be used to obtain discrete points along the stress-strain curve [20–25]. However, this study will focus on a nanoindentation approach utilizing spherical tips which cause a non-self-similar stress field under the tip and thus induce a continuously increasing representative strain with increasing indentation depth. Numerous advances have been made in the analysis of spherical indentation curves since Tabor stated in the early 1950s that the hardness can be related to the stress of uni-axial flow curves [21,26]. The present study will revisit spherical indentation approaches and essentially refine and extend existing procedures to lastly enable this technique to serve as an equivalent to elaborate micromechanical uniaxial testing methods such as micropillar compression [27]. For this purpose, new calibration procedures will be introduced which allow the depth-independent determination of the Young's modulus despite tip imperfections. Subsequently, the importance of constant strain-rate experiments will be highlighted, accompanied by a comparison of existing standard testing protocols. We will demonstrate that the presented refinements facilitate the reliable determination of rate-dependent properties by using both, a constant strain-rate approach or strain-rate jump tests, respectively. Finally, scaling the constraint factor in an experimentally informed manner by utilizing the ratio of unloading and loading slopes of nanoindentation load-displacement curves will provide a physically based concept to convert spherical nanoindentation data to flow curves that are in excellent agreement with uniaxial tests.

1.1. State-of-the-art nanoindentation analysis for spherical indentation

Numerous studies have been published in the past decades which perceptibly advanced spherical nanoindentation approaches [13,21,26,28–38]. Progresses shall briefly be summarized at this point.

Nowadays, the Meyer's hardness is widely considered as appropriate definition of H, where the projected area is used [39] instead of the area in touch with the sample commonly used in Brinell tests. Furthermore, the elastic distortion contribution which can be significant in small scale tests, is accounted for and consequently allows to separate plastic and elastic regimes from load-displacement data at maximum load [2–4,6,13]. Still, elastic deformation during loading may change the corresponding area in contact, hence an effective radius can be used to take this issue into account [33,34]. Kalidindi and Pathak made use of dynamic indentation protocols where they evaluated the contact area A_c from the stiffness of isotropic samples (reduced modulus E^* is constant) [29–31] based on the equation derived by Sneddon [4].

$$E^* = \frac{\sqrt{\pi}}{2} \cdot \frac{S}{\sqrt{A_c}}, \tag{1}$$

with S as the stiffness, and thus could indicate tip shape problems. Additionally, they redefined the representative indentation strain to [29–31].

$$\varepsilon_i = \frac{4 \cdot h}{3 \cdot \pi \cdot a_c}, \tag{2}$$

with h as the total displacement and a_c as the contact radius, which can be derived from Hertz's law for elastic contact in contrast to the empirical relation from Tabor [21].

$$\varepsilon_i = 0.2 \cdot \frac{a_{(c)}}{R_{(eff)}}, \tag{3}$$

with $R_{(eff)}$ as the radius or effective radius [33,34] of the tip and $a_{(c)}$ as the contact radius or the radius of the residual impression. Both lead to a dependency of the opening angle with respect to a certain displacement. By applying a zero-point correction in the elastic regime to exclude effects from surface artefacts, one can obtain the effective point of initial contact, providing a correct elastic Hooke's line in the determined indentation stress-strain curves [29–31].

The determination of the representative indentation stress σ_r is challenging. A linear conversion between the mean pressure or hardness, respectively, and stress has been suggested by Tabor [21]:

$$H = C^* \cdot \sigma_r, \tag{4}$$

where C^* is the constraint factor.

However, nowadays there is general agreement in literature [13,20,21,32,40–46] that C^* itself depends on the ratio E^*/σ and the indentation strain, and that it increases with increasing strain and E^*/σ values up to a plateau-value of around 3.

2. Testing setup & used samples

Nanoindentation experiments of the present study were performed on a Keysight G200 with integrated continuous stiffness measurement (CSM) unit. Dynamic measurements were carried out with a displacement amplitude of 2 nm oscillating at 45 Hz in order to minimize errors caused by the system's lock-in amplifier [47]. It is important to note that by using the CSM unit the hardness can be obtained over displacement and hence hardness values correspond to the set strain-rate. This is not the case for H values obtained with multiple unloading tests, where the strain-rate drops in the hold regime of each cycle and might falsify results of rate-sensitive materials [48]. All nanoindentation tips were obtained from Synton MDP LTD, Nidau, Switzerland. For reference measurements, a Berkovich diamond tip was used for 2500 nm deep indentations with a set strain-rate of 0.05 s^{-1} to determine hardness and Young's modulus according to the conventional analysis of Oliver and Pharr [2]. Berkovich strain-rate jump tests [49] were performed using strain-rates of 0.05 s^{-1}, 0.005 s^{-1} and 0.001 s^{-1} for displacement regimes of 500 nm each. Top-ground diamond cone tips with a half

opening angle of 45° were used as spherical tips with specified radii R_{spec} ranging from 5 μm to 60 μm. Mentioned radii in the text refer to the R_{spec} of the corresponding tip. Strain-rate profiles for spherical tip experiments will be presented below. Thermal drift was measured in a post-test segment at 10% of the maximum load and did not exceed 0.2 nm/s for any indent. The data acquisition rate was set 5 Hz. At least six indents were performed for each parameter set, and in the following figures representative results will be shown.

Micropillars used for comparison of uniaxial flow characteristics were milled with a Ga focused ion beam with an aspect ratio of 2.5 to 3. Taper-free rectangular UFG W (3.5×3.5 μm^2) and UFG Cr (3.5×3.5 μm^2) were fabricated in a dual-beam SEM-FIB (Zeiss LEO 1540 XP, Oberkochen, Germany). Details and corresponding stress-strain curves were previously reported from by Fritz et al. [50,51]. Cylindrical NC Ni ($\varnothing$ 4.5 μm) and UFG Cu ($\varnothing$ 4.9 μm) were prepared by annular milling (Zeiss Auriga Platform, Oberkochen, Germany) and tested at the G200 nanoindenter using a diamond flat punch as tip ($\varnothing$ 10) μm and utilizing a goniometer based stage as suggested by Uchic and Dimiduk to correct for misalignments [52]. No sample size effect is expected due to reduced grain sizes of theses samples combined with rather large pillar dimensions [53–55].

The suitability and requirements of tested materials shall briefly be discussed at this point. The presented tip calibration is universally applicable and not restricted to an internal length scale. The material selection for this part includes glassy carbon, fused quartz (FQ), fine-grained (FG, grain-size (GS): 1.05 μm $\pm$ 0.25 μm) 6014 Al-alloy, ultrafine-grained (UFG, GS: 0.28 μm $\pm$ 0.14 μm) copper, nanocrystalline (NC, GS: 30 nm) nickel, UFG (GS: 0.3 μm $\pm$ 0.1 μm) chromium and UFG (GS: 0.89 μm $\pm$ 0.51 μm) tungsten. This selection includes amorphous, face-centered cubic (FCC) and body-centered cubic (BCC) materials of varying grain-size. For investigations of strain-rate effects the accumulative roll bonded (8 repeats) 6014 Al-alloy [56] was used since its enhanced strain-rate sensitivity m will contribute to clearly visible implications. Furthermore, constant strain-rate tests were conducted on a (100)-oriented GaAs wafer due to its homogeneity and pronounced pop-in effects [57,58].

Despite the undisputable benefits of spherical indentation, some challenges come along with its use as characterization technique, as the obtained properties also depend on the microstructural dimensions of the tested material. Size effects referring to the sphere radius for coarse grained structures complicate the extraction and flow curves and cannot easily be subtracted from the data. However, most modern materials make use of reduced internal length-scales which lead to enhanced strength while maintaining sufficient ductility [59–62]. In terms of flow curve extraction, this study aims to extract nanoindentation flow curves for ultra-fine grained and nanocrystalline materials where loaded volumes are representative already at shallow indentation depths. Hence, anisotropy and indentation size effects will only play a negligible role. NC Ni, UFG Cu, UFG Cr and UFG W, spanning in grain-size from ~30 nm to ~1 μm, were used for flow curve extraction experiments.

3. Novel methodical approaches

Subsequent paragraphs deal with refinements and extensions of current spherical nanoindentation protocols. New tip calibration approaches and strain-rate controlled experiments detailed here will serve as a solid base for the reliable extraction of spherical nanoindentation flow curves later.

3.1. Tip calibrations

Fabrication of spherical tips using hard and stiff materials, such as diamond or sapphire, is an ambitious task since these materials are predominantly anisotropic. Even though deviations from the specified shape are generally small, they may cause major problems in nanoindentation experiments. For instance, the correct tip shape will be needed to conduct constant strain-rate tests, as the strain depends on the ratio between displacement and contact radius according to Eq. (2). To overcome tip shape problems, one principle idea is to replace the specified radius with an effective radius to extend the applicability of the calibration to the elastic-plastic regime [33,34]. Back-calculating the contact area from the stiffness signal (see Eq. (1)) is an appropriate approach but requires a priori knowledge of E^* and adds perceptible noise to the data [12,29–31,63].

Analysis of 3D profiles recorded by a laser confocal microscope (Olympus LEXT OLS4100, Tokyo, Japan) reveals the non-perfect tip shape of a new spherical tip (Fig. 1a). An SEM image (see inlay of Fig. 1b) of the spherical tip shows that the body is rather an ellipsoid than a spherical segment which should be considered in the analysis. Hence, the use of a single number for the radius of a tip is insufficient. Still, R$_{spec}$ will be referred to keep the tips assignable, but only serves as a rough qualitative number of the tip dimension which will not be used in any analysis. Alike sharp indenter tips, one preferably calibrates each tip to obtain individual area functions using an elastically isotropic material such as fused quartz. For sharp tips, this can accurately be done using the series [2].

$$A_c(h_c) = \sum_{i=0}^{i} B_i \cdot h_c^{1/2^{i-1}}. \tag{5}$$

Considering a perfect tip, the geometry constants B_1 to B_i become zero and $B_0 = 3 \cdot \sqrt{3} \cdot tan^2(\alpha)$, where α is the complementary angle between the normal vector of the pyramid face and the loading direction. This function type is notably useful for sharp tips since the terms after the lead term will mainly account for tip imperfections at shallow depths which is the most problematic regime for sharp tips. Nevertheless, it turns out that this approach is not as reliable for spherical tips because these tips differ in their sphericity. Hence, the shape can also crucially deviate at large displacements, which is the reason why a geometry-based area function should be favored. Basic geometrical considerations allow to express the area as a function of the displacement, using following equations with a as the radius of the projected area, R as the sphere radius and h as displacement:

$$A = 2 \cdot a \cdot \pi, \tag{6}$$

$$a^2 = 2 \cdot R \cdot h - h^2. \tag{7}$$

Combining these equations, and considering the real area in contact instead of the total displacement [2], indicated by the index c, this leads to

$$A_c(h_c) = B_0 \cdot h_c^{B_1} - B_2 \cdot h_c^2, \tag{8}$$

which properly describes a perfect sphere if $B_0 = 2 \cdot R \cdot \pi$, $B_1 = 1$ and $B_2 = \pi$. To describe imperfect tips, the constants B_i can be varied using a non-linear least square method. Note that the variation of one exponent is important to vary the sphericity of the tip shape. Another fundamental asset of using this type of function is that starting values for the parameters B_i in these non-linear least square methods have a physical meaning as they refer to the radius of the idealized tip. Consequently, this leads to faster convergence and high numeric stability of the procedure. Still, fitting parameters may slightly differ depending on the least-square method. In this study, a Levenberg-Marquardt algorithm [64,65] (routine implemented in the Python package SciPy) was used for this purpose and consistently provides satisfying results yielding coefficients of determination >0.985 for any conducted calibration. Generally, as the tip shape itself differs from that of a sphere, the current analysis based on Sneddon's studies should be favored [4] which is analogue to the widely accepted calibration method proposed by Oliver and Pharr [2]. Compared to Hertzian analysis [33,34,66] there is no need to extend
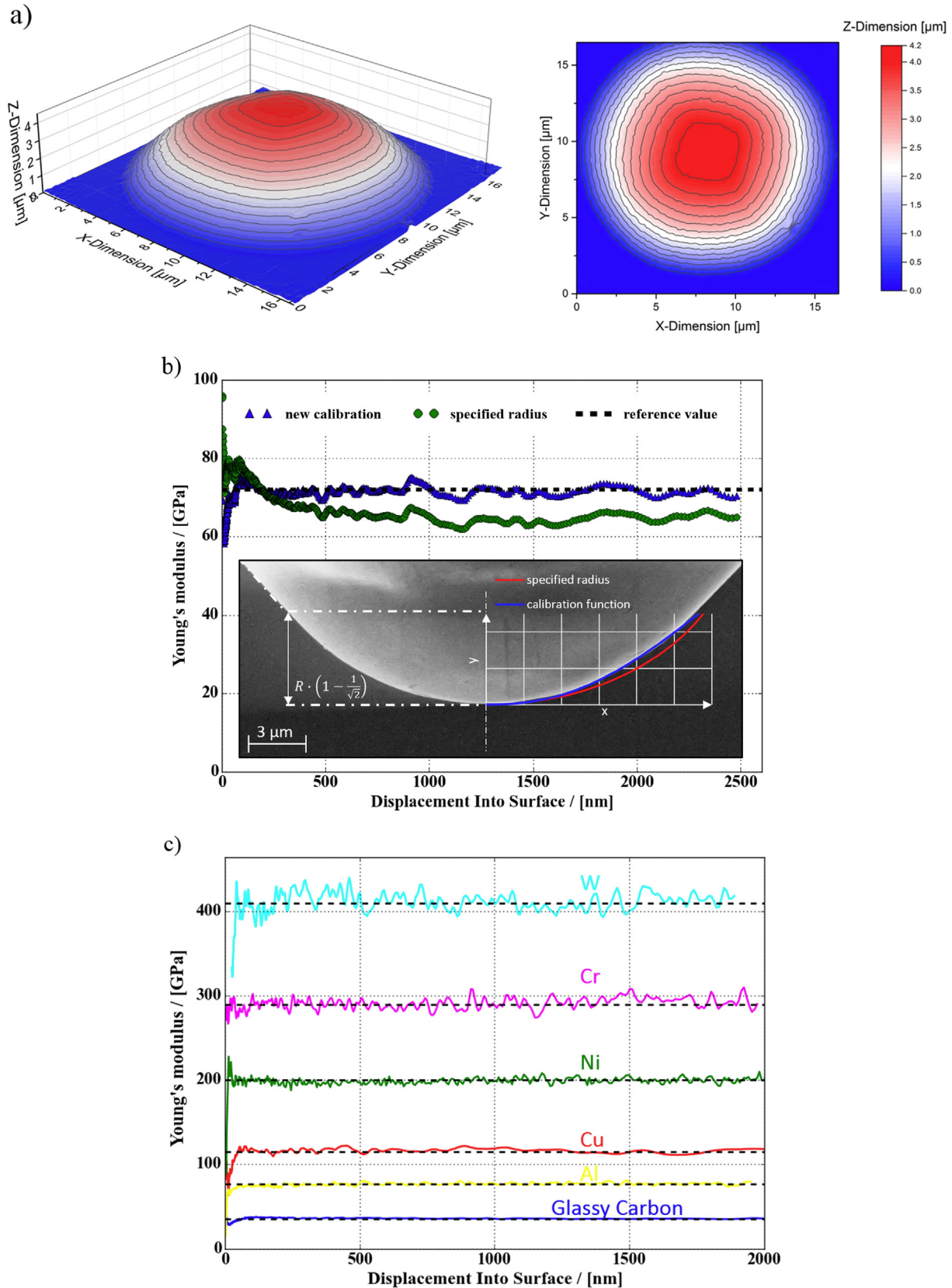
Fig. 1. a) 3D profile of a spherical tip obtained by a laser confocal microscope reveals the non-perfect tip shape. b) Profile of the Young's modulus of FQ over displacement using the specified tip radius (green circles) to calculate the contact area and using the described new calibrated area function (blue triangles). The inset SEM micrograph of a spherical tip ($R_{spec} = 20\,\mu m$) shows the limit of the spherical shape and that in contrast to a perfect sphere the new area function matches the tip contours well. c) Horizontal profiles of the Young's modulus on various isotropic materials indicate valid measurements for samples with a broad spectrum of E ranging from 35 GPa (Glassy Carbon) to 400 GPa (W). The black dashed lines represent reference Berkovich values for the tested materials.

the analysis to the plastic regime where the curvature of the residual indent has to be approximated. Another benefit of this highly accurate 3-parameter function is that a fast feedback can be realized that allows to set relatively high strain-rates as will be shown in the next section.

However, one should not forget that spherical tips are often made from a cone as semifinished part. If the total opening angle of the base-cone is 90°, as it is the case in this study, a spherical shape can only be provided up to a displacement of $h = R \cdot (1 - \frac{1}{\sqrt{2}})$, indicated in Fig. 1b. At this point the slope of the sphere tangent matches the cone half angle and for larger displacements indentation strain will not increase anymore.

Correct calibrations are confirmed by horizontal profiles of the Young's modulus over displacement. Fig. 1b shows a comparison between doubtful results obtained using the specified radius, and parameters from the new calibration procedure, which is well in agreement with literature values for fused quartz [2]. Even if the specified radius would be replaced by a slightly smaller radius this would only lead to a parallel translation of the green curve and still exhibit the strong unphysical gradient in modulus at shallow depths. Elastic distortions or material pile ups around the indent may occur depending on the material. Regrettably, one cannot entirely exclude this effect, but Fig. 1c clearly demonstrates that E-values, spanning from 35 GPa to 400 GPa, are conform with reference values obtained by Berkovich tests and literature data [2,67,68], thus pile-up and sink-in behavior seem to be of minor importance.

Once the real tip shape is known, due to this improved calibration the influence of different strain-rates can be investigated as will be done in the following section.

3.2. Strain-rate controlled experiments in spherical indentation

In most modern high-performance metals deformation is not simply governed by athermal dislocation plasticity, but rate-dependent mechanisms are responsible for high strength properties. Thus, controlling the strain-rate in experiments is crucial to obtain useful flow curves. For nanoindentation tests the definition of the strain or strain-rate, respectively, is not straightforward and certainly depends on the used tip. The definition of the strain for spherical tips has been discussed several times in the past, however, the definition used by Pathak and Kalidindi [29–31] seems currently to be the most convincing one. In their spherical nanoindentation study, they could demonstrate that the expected Hooke's line can be measured for W and Al single crystals prior to pop-in events. The advantage of only considering the elastic regime is clearly that the hardness is conform with the stress in the material, since the hydrostatic pressure contributes to elastic deformation.

The strain is given by Eq. (2). Naturally, the load-time profile in nanoindentation tests must be adapted to this definition to guarantee a correct strain-rate. Nanoindentation devices are often load-controlled, hence controlling via the time derivative of Eq. (2) can be challenging. Feldner et al. first addressed the problem of a varying strain-rate during spherical indentation [37]. They used Eqs. (1) & (2) combined with the assumption of an elastic contact and a perfect sphere to end up in a strain-rate proportional to $\dot{P}/P^{2/3}$, with $\dot{P}$ the time derivative of the load. This parameter is similar to that used in sharp indentation experiments ($\dot{\varepsilon}_{sharp} = \dot{P}/P$) to tune the strain-rate [37,69] and easily controllable with the used indentation device. Even though this reduces the strain-rate induced error, the assumptions impair the success of the approach.

Within this study, we successfully implemented strain-rate controlled experiments according to the strain definition of Eq. (2) over a few orders of magnitude by tuning the proportional-integral-derivative parameters of the integrated PID-control. The proposed area function in beneficial in this context as a simple form favors a fast PID-feedback and thereby allows to reach relatively high strain-rates. Furthermore, by our definition also tip imperfections are considered

a)

b)

c)
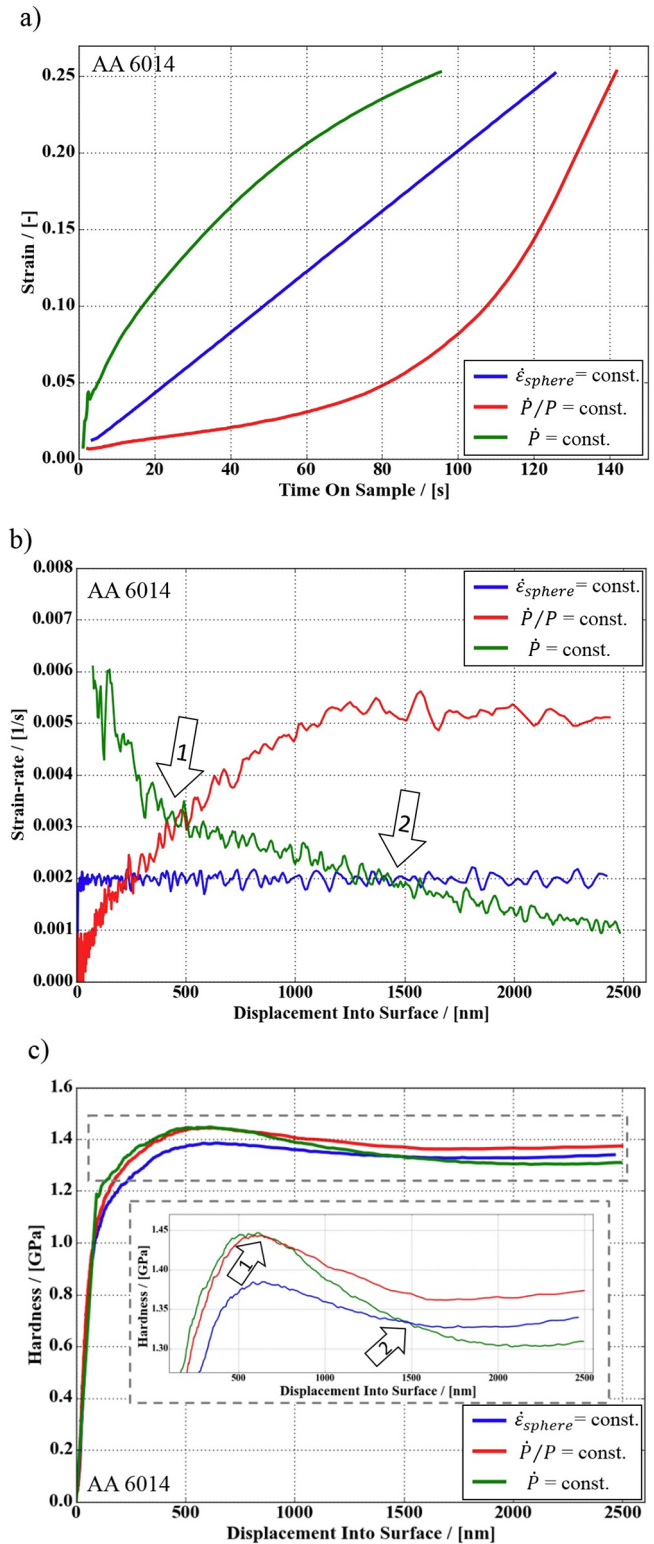
Fig. 2. a & b) Temporal profiles of the indentation strain show the linear increase for cSR tests (blue) yielding to constant strain-rate while cLR (green) and $\dot{P}/P$ (red) experiments end up in a continuously decreasing and increasing strain-rate, respectively. c) Resulting hardness curves of the 6014 Al-alloy demonstrate the strong dependence of the strain-rate for spherical tests. Intersects of the hardness match the intersects of the strain-rates in b).

for a correct strain-rate. This aspect is often neglected in sharp tip indentation as $\dot{\varepsilon}_{sharp} = \dot{P}/P$ actually refers to a perfect self-similar tip but seem

to have a minor impact since pyramidal tip shapes are close to specifications. For spherical indentation, achievable strains and strain-rates depend on the radius and area function of the sphere. Fig. 2a–c display strain, strain-rate and hardness profiles for different testing methods measured with a 5 μm radius tip according to specifications. Constant strain-rate experiments at 0.002 s^{-1} have been performed accompanied by a linear increase of strain over time (Fig. 2a) and a constant strain-rate in Fig. 2b. Using the definition for sharp indenter tips ($\dot{P}/P$ = const.) and a set strain-rate 0.05 s^{-1} leads to a continuous increase of the strain-rate over displacement, while the strain-rate of constant load-rate (cLR) experiments using 0.75 mN/s are monotonically decreasing. Fig. 2c shows the corresponding hardness profiles which go along with the strain-rate profiles of Fig. 2b. One can see in the magnified inset that the cLR hardness curve at first intersects the profile which uses the strain-rate definition of sharp tips ($\dot{P}/P$ = const.) at about 500 nm (arrow 1) and subsequently the profile of constant strain-rate (cSR) tests at around 1500 nm (arrow 2) just as it happens for the strain-rates in Fig. 2b. As one might expect, when tested at the same strain-rate the flow stresses match. Fig. 2c thereby evidences that work hardening behavior obtained from spherical indentation will significantly be falsified if the strain-rate is not adequately

considered for rate sensitive materials making the implementation of cSR tests crucial for any spherical indentation study dealing with rate-sensitive materials such as bcc or nanocrystalline metals. However, only for the cSR data the strain-rate is constant throughout the test. Note that the inputs for load-rate, sharp tip strain-rate and spherical tip strain-rate have been chosen to come down to similar testing times. Independent of the absolute input values all trends will remain the same.

Once the strain-rate is properly considered, spherical indentation experiments turn out to be extraordinarily stable and reliable. Note the marginal deviations in Fig. 3a which displays the hardness curves of three indentations performed with a 10 μm radius tip on NC Ni at a strain-rate of 0.0005 s^{-1}, resulting in testing times of about 360 s. For spherical nanoindentation of coarse grained materials, the measured hardness values depend on the tip radius, where conventionally smaller radii lead to higher hardness values [18]. In contrast to the ISE known from self-similar tips, the size effect is not influenced by the current displacement or load but must be investigated at coinciding representative strains [17,18,70]. This well-known tip size effect of coarse grained materials is attributed to geometric necessary dislocations which need to be created to accommodate the tip in the material. This model assumes that dislocation loops form around the penetrating tip [14,18]. For the materials with small grain sizes this effect can be excluded as the length of dislocation loops by far exceeds the microstructural dimensions also at shallow depths. Fig. 3b demonstrates that for NC Ni, where representative volumes are tested instantaneously, tip size effects are negligible since spherical tips with radii of 10 μm, 20 μm and 50 μm lead to matching hardness profiles.

3.3. Rate-dependent properties

Understanding spherical indentation and controlling the strain-rate enables the method to characterize samples regarding thermally activated mechanisms. Considering Eq. (4) and assuming C^* constant at a representative strain, one can proof the equivalence between the logarithmic hardness and representative stress difference, respectively:

$$\Delta \ln H = \ln H_2 - \ln H_1 = \ln(\sigma_2 \cdot C^*) - \ln(\sigma_1 \cdot C^*)$$
$$= \ln(\sigma_2) + \ln(C^*) - \ln(\sigma_1) - \ln(C^*) = \Delta \ln \sigma, \qquad (9)$$

which finally allows to calculate the strain-rate sensitivity m according to [71,72].

$$m = \frac{\Delta \ln \sigma_r}{\Delta \ln \dot{\varepsilon}} = \frac{\Delta H}{\Delta \ln \dot{\varepsilon}}. \qquad (10)$$

Different approaches can be used to determine the strain-rate sensitivity or activation volume of a material. On the one hand, various indents with different constant strain-rates can be executed, which is time consuming but allows determining m in dependence of the imposed strain. To verify this method, a GaAs wafer was used in this study since the properties of this material are well suited to double-check the reliability. The sample features an enhanced strain-rate sensitivity but is additionally highly homogeneous and contains few defects. Hence, distinct pop-ins are expected, which will indicate the start of plastic deformation [57,58]. Up to this point, the deformation will be purely elastic and consequently the hardness or stress values, respectively, should not differ in dependence of the used strain-rate. Additionally, stress-strain profiles should accord to Hook's line and comply with the Young's modulus measured by the CSM signal or with measurements from standard Berkovich indentation. After the point of yield, a significant difference in hardness is expected, depending on the strain-rate. Fig. 4a demonstrates cSR tests conducted with a 5 μm radius tip on GaAs. Just as expected above, the indentation data exhibits all the features mentioned above for indents performed with strain-rates of 0.01 s^{-1}, 0.001 s^{-1} and 0.0005 s^{-1}. Consistent Hooke lines also ensure
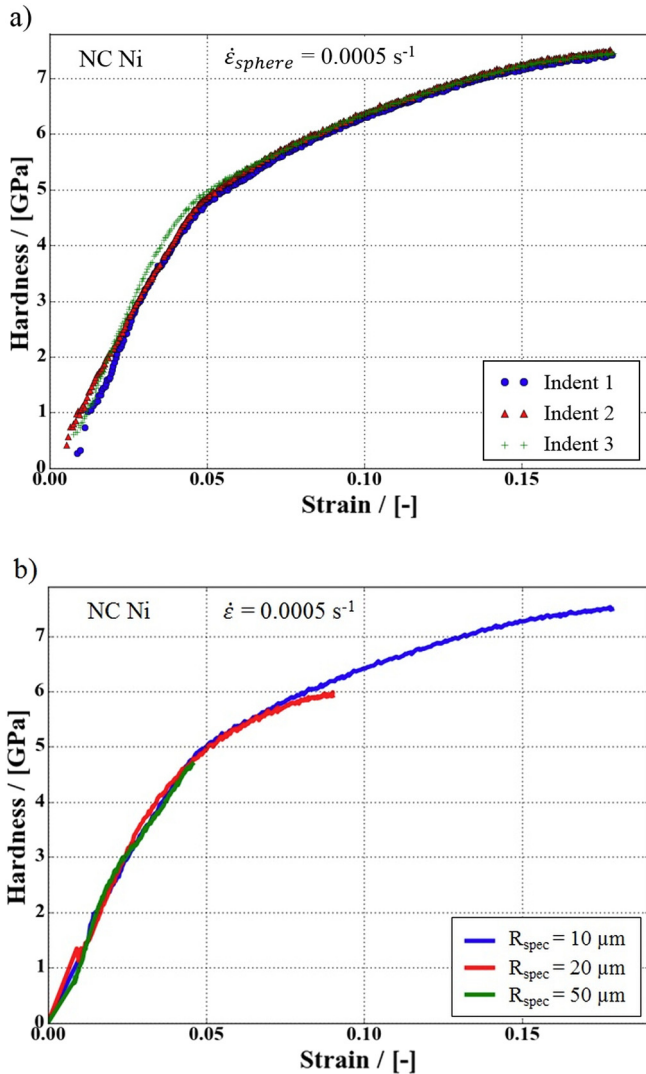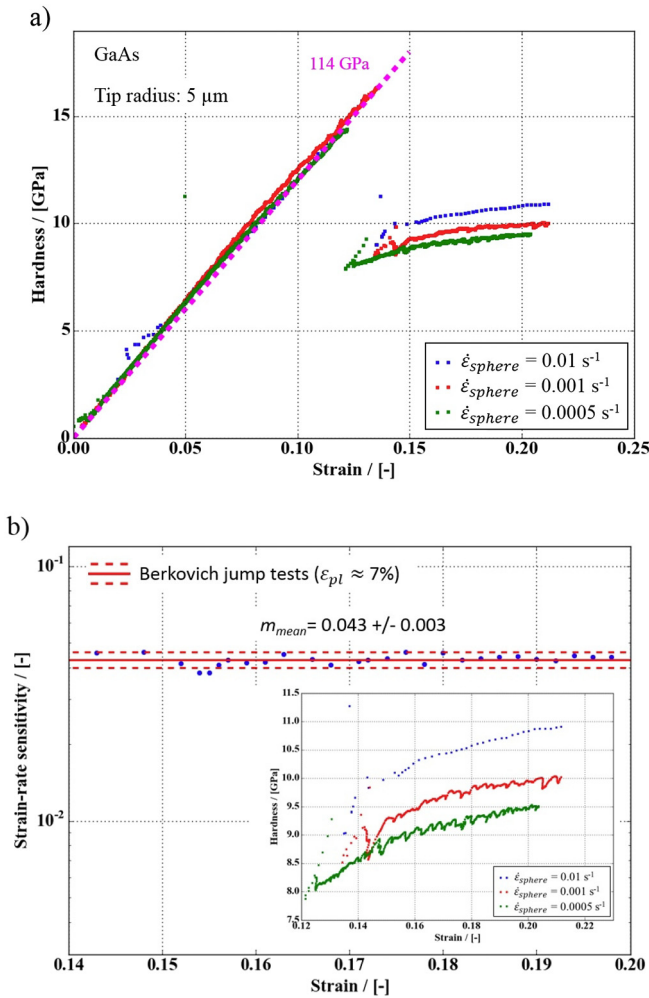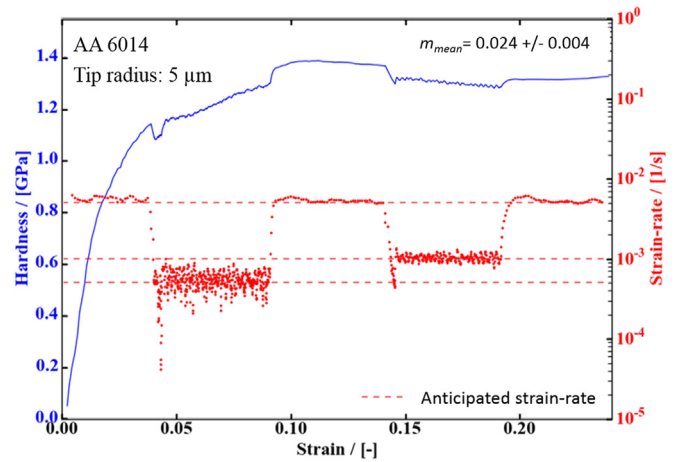
Fig. 3. a) Hardness curves of three different indents on NC Ni illustrate the high reliability of the technique. b) Hardness-strain profiles obtained on NC Ni with three different indenter tip radii using a strain-rate of 0.0005 s^{-1} verifies that mechanical properties can be determined independent of the used radius.

a)

b)

Fig. 4. a) Hardness over indentation strain for experiments on GaAs. During the elastic loading prior to pop-in events the hardness is equal to the stress, thus Hooke's line with the corresponding Young's modulus of 114 GPa is imprinted as a dashed line. In the plastic regime after pop-in, magnified in the inset in b), a distinct rate-dependence can be noted. Analysis of m over strain shows a strain-independent value of 0.043, conform with Berkovich jump tests ascribed to a representative strain of 7%.

Fig. 5. Spherical indentation strain-rate jump tests for an ARB Al alloy (6014). The strain-rate profiles (red dots) clearly demonstrate that the anticipated strain rates (red dashed lines) are reached for every segment of 5% strain.

dependable analysis of m since strain-offsets could significantly change results. Fig. 4b shows that the strain-rate sensitivity determined using the 0.01 s^{-1} and 0.0005 s^{-1} data is constant over strain. Hence, Berkovich nanoindentation jump tests, ascribed to a representative strain of around 7%, can be well compared to spherical experiments, all of which resulting in the same m-value of 0.043 ± 0.003. Notably, for the sphere only values starting from 14% strain can be used since the rapid pop-in process causes slight deviations from the anticipated strain-rate before.

Elaborate test schedules are necessary to gain rate-dependent properties using the cSR method at different rates. However, strain-rate jump tests can now also be implemented for spherical indentations as already demonstrated by Feldner et al., even though they had a challenging situation since they calculated the contact radius from the stiffness assuming a constant modulus [37]. This goes along with distinct noise of the stiffness signal and complicates the analysis of the strain-rate jumps. Within this study, using the new calibration procedure, we can avoid this problem and extend the technique also to materials with unknown or varying elastic properties. Fig. 5 shows a hardness-strain plot for an ARB FG Al-alloy (6014) which, as common for refined FCC metals, shows a pronounced strain-rate sensitivity. The GaAs SX

sample is not suited for this testing method as the pop-in occurring at rather high strains impedes the use of multiple strain-rate regimes required for the analysis. Red dots indicate the strain-rate during the tests while the red dashed line highlights the levels of the anticipated strain-rates of 0.005 s^{-1}, 0.001 s^{-1} and 0.0005 s^{-1}, which are constantly achieved. Solely during slowing down the strain-rate slight undershoots can be noted. Analysis of nine jump tests, only considering the last three jumps each, ends up in 27 hardness/strain-rate pairs which lead to an m-value of 0.024 ± 0.004, conform to values obtained by reference Berkovich jump tests of 0.024 ± 0.002.

4. Flow curve extraction

After ensuring reliable measurements by knowing the actual tip shape and controlling the strain-rate, the implication is to transform the hardness-strain profiles to stress-strain curves also in the plastic regime. This demanding task has been attempted several times before, also including FEM simulation supported methods [13,20,21,32,40–46]. The international organization of standardization (ISO) addressed this topic in a comprehensive technical report [73], even though aspects such as tip imperfections and strain-rate effects are not considered and the suggested methods to link indentation to uniaxial properties always rely on computational techniques. Extensive experimental approaches on samples with small internal length-scales, where size effects are insignificant, are seldom. And ideally, uniaxial compression tests should be performed on the identical sample for comparison. The main difficulty towards unambiguous flow curves from indentation is the conversion from hardness to a representative indentation stress value even though it has often been demonstrated that this constraint factor C^* is in the order of 3 for metals. As mentioned above, the constraint factor varies dependent on elastic (E^*) and plastic properties (yield stress σ_y) as well as the indentation strain. The value of the representative strain varies depending on the used definition (Tabor [21] or Kalidindi and Pathak [29]), but scales with cot Θ, where Θ is the opening angle of the tip at a certain displacement (details see Appendix A). Table 1 gives an overview of C^* dependencies in literature for both spherical and sharp indenter tips, neglecting effects from work hardening or friction.

In some studies, differentiation whether the constraint factor links the hardness to the stress at the representative strain or to the initial yield stress of a material is not obvious. Most of the approaches require an a priori knowledge of the yield stress of the sample, which would certainly be a shortcoming of the used spherical indentation approach.

Table 1
Dependencies of the indentation constraint factor used in previous studies.

Authors	Dependency of C^*
Tabor [20]	$C^* = const.$
Johnson [13]	$C^* = f(\frac{E^*}{\sigma_y} \cdot \cot\theta)$
Fleck and Mesarovic [31]	$C^* = f(\frac{E^*}{\sigma_y} \cdot \frac{2 \cdot \cot\theta}{1 + \cot^2\theta})$
Hay et al. [40]	$C^* = f(\frac{E^*}{H} \cdot \cot\theta)$
Park and Pharr [22]	$C^* = f(\frac{E^*}{\sigma_y} \cdot \frac{2 \cdot \cot\theta}{1 + \cot^2\theta})$
Mata et al. [43]	$C^* = f(\frac{E^*}{\sigma_y} \cdot \cot\theta)$
Kang [45]	$C^* = f(\frac{E^*}{\sigma_y} \cdot \frac{2 \cdot \cot\theta}{1 + \cot^2\theta})$
Chen and Vlassak [66]	$C^* = f(\frac{E^*}{\sigma_y} \cdot \cot\theta)$
Rodriguez et al. [44]	$C^* = f(\frac{E^*}{\sigma_r})$

Fig. 6. Experimental dependency of the constraint factor C^* on μ (blue circles) determined by the comparison of uniaxial and spherical indentation flow curves on NC Ni. Fitting functions (dashed line) according to Eq. (12) for the four different observable deformation regimes.

Only Hay et al. [41] and Rodriguez et al. [45] linked C^* to the representative stress or hardness, respectively. The parameter used by Hay et al. [41] is particularly appealing, as it is directly related to the plastic and elastic work introduced and clearly distinguishes the elastic and plastic regime. Furthermore, it can be experimentally obtained from indentation measurements if CSM is used by calculating the ratio of the contact stiffness S and the slope of the load/contact depth curve n_L, called μ in this study
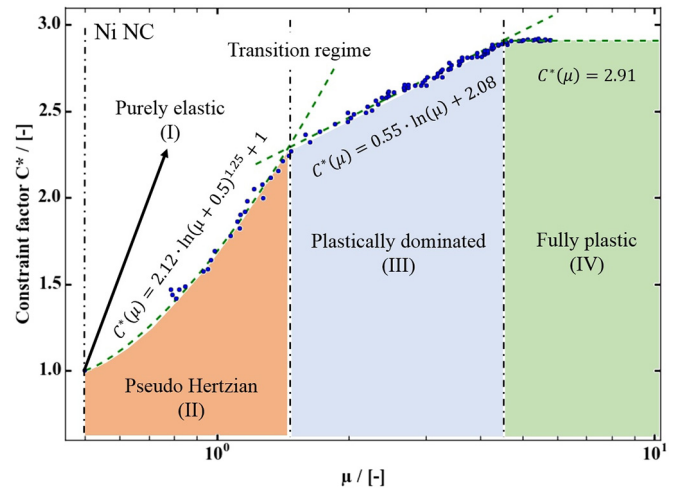
$$\mu = \frac{S}{n_L} = \frac{E_r}{H} \cdot \frac{\cot\theta}{\pi}. \tag{11}$$

See Appendix B for details. This parameter was also identified by Johnson to be proportional to the plastic zone size occurring during indentation [13]. It can be converted to the dimensionless parameter $\frac{E_r}{\sigma} \cdot \frac{a_c}{R}$ (see Appendix A) which has been identified to have a major impact on the value of C^* [13,32,44,46,74].

Uniaxial tests will now be used to determine a genuine function for $C^* = f(\mu)$ for spherical indentation experiments on pillars. This function can be determined by matching the indentation flow curve to the uniaxial pillar flow curve. For this purpose, the stress-strain curve from pillar compression tests and hardness-strain curves from spherical indentation tests were subdivided in strain increments $\Delta\varepsilon$ of 0.001 and used for the calculation of C^* according to Eq. (4). A 10 μm radius tip and NC Ni have been used for this procedure, since deformation will then mainly take place in the elastic-plastic transition regime, but also reaches the fully plastic regime at high strains. Considering the elastic/plastic work ratio μ yields in the profile depicted in Fig. 6, which is in accordance to the expected shape from FEM studies [32,74], can be subdivided in four regimes as firstly suggested by Park and Pharr [74]. Using μ, reduces the purely elastic state (I) to a single point at $\mu = 0.5$ and $C^* = 1$. Increasing the strain puts the deformed volume in the transition regime which is at first elastically dominated (pseudo Hertzian (II), see [74]) and then abruptly changes to a plastically dominated behavior (III). Finally, at large strains, favored by high E/σ values, a fully plastic regime can be observed (IV) where C^* becomes constant and from which Tabor's proposal of a $C^* = const.$ might originate from. The profile can be split and expressed as an empiric function:

$$C^*(\mu) = \begin{cases} 1 & , \mu = 0.5 & (I) \\ 2.12 \cdot \ln(\mu + 0.5)^{1.25} + 1, & 0.5 < \mu < 1.45 & (II) \\ 0.55 \cdot \ln(\mu) + 2.08, & 1.45 \le \mu < 4.5 & (III) \\ 2.91 & , x \ge 4.5 & (IV) \end{cases} \tag{12}$$

By this function, one can determine the constraint factor profile for each indent, since μ can directly be evaluated from the nanoindentation device. Studies showed that for materials with similar work hardening behavior and frictional properties, the same function will be applicable [32,74]. The used materials (NC Ni, UFG Cu, UFG Cr, UFW W) will fulfil these qualifications. Fig. 7a–d shows the comparison of flow curves
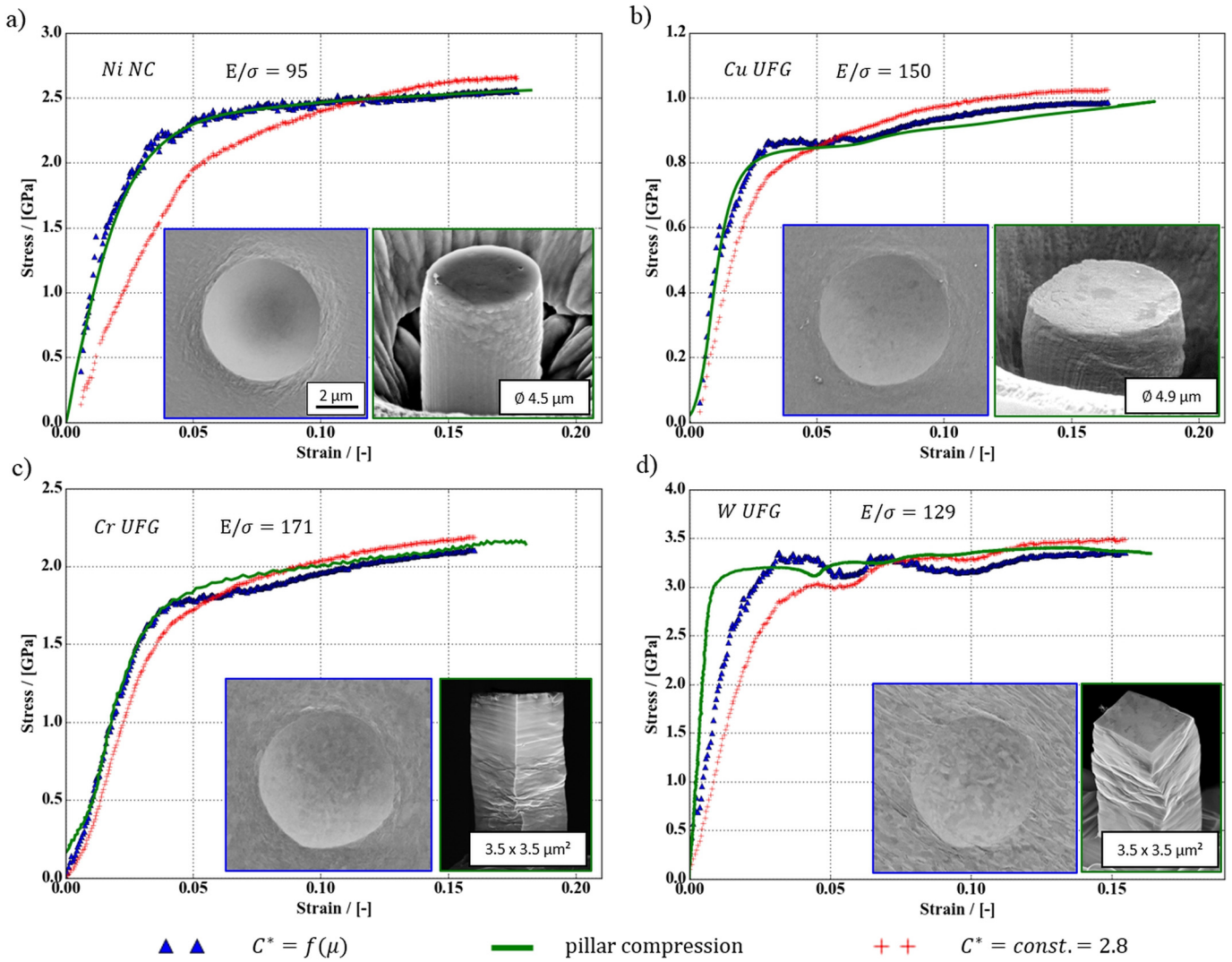
obtained by pillar compression tests (green solid line) and spherical indentation experiments with variable C^* (blue triangles). Additionally, stress-strain curves using the original approach of Tabor with a constant constraint factor of 2.8 [21] are imprinted (red crosses), which clearly underestimate the yield level and overestimate the work-hardening of the materials. Obviously, the match in Fig. 7a is self-explanatory since these curves were used to obtain the function for C^*. However, also Fig. 7b–d show excellent agreement, which make the assumptions seem justified once materials with reasonably similar mechanical character are tested. Interestingly, also instabilities during compression, as occurrent for UFG W in Fig. 7d were individual grains yield, are picked up in spherical indentation experiments. Notably, the difference between the red and blue curves is more significant for materials where E/σ is low. Here values for C^* will refer to low values of μ and consequently noticeably deviate from the constant value of 2.8 (see Fig. 6). Tabor might have unintentionally avoided this problem, since he tested coarse grained mild steel and copper that both feature high values of E/σ > 400. Additionally, one must not forget that Tabor calculated the hardness by dividing the load by the area of the residual imprint, which will slightly deviate from the projected area at maximum load.

5. Summary and conclusion

Few experimental techniques feature the enormous efficiency and capability for the substantial characterization of materials as is the case for spherical nanoindentation. Despite these outstanding perspectives current instrumented indentation methods do not have the precision which is required for excellence in material science and quality management. Within this study we present a wide variety of significant advances which should be adapted to existing nanoindentation protocols.

i. The calibration of spherical tips has been reinvestigated. Based on the geometry of a sphere, a novel non-linear function type is suggested to calculate the contact area in dependence of the contact depth, which allows to account for deviant sphericity also at large displacements. The accuracy of the introduced highly stable fitting procedure was validated on a broad spectrum of materials with Young's moduli ranging from 35 GPa to 400 GPa. This approach also impedes the problem of signal noise which occurs if the stiffness is used to back-calculate the current contact area function.

Fig. 7. Comparison between uniaxial micropillar compression tests (green solid line) and spherical indentation flow curves using a constant constraint factor of 2.8 (red crosses) and a variable constraint-factor (blue triangles) for NC Ni, UFG W, UFG Cr and UFG Cu. Insets show SEM micrographs of spherical impressions (scale-bar of a) applies to all indentations) and post-mortem pillars of the corresponding material.

ii. Adequately controlling the strain-rate is challenging for spherical indentation since the strain will be influenced by tip shape imperfections and an assumed constant radius is a deficient approximation for rate-dependent modern high-performance materials. Tuning the PID-parameters of the used nanoindentation device allows to exactly achieve set strain-rates and eliminates impacts of the actual tip shape. Comparison to constant load-rate and constant strain-rate tests used for pyramidal tips show that these strain-rate profiles would significantly falsify the appearance of hardness curves.

iii. Performing experiments with constant strain-rates shows that materials with refined microstructures, ensuring the instantaneous sampling of a representative volume, do not feature a tip size effect and exhibit formidable reproducibility.

iv. Properly controlling the strain-rate opens the door to extract the strain-rate sensitivity either by constant strain-rate experiments or by spherical nanoindentation jump tests. Values are in excellent agreement with data obtained by sharp tip indentation and do not show a strain dependence.

v. A novel approach to account for a physically realistic varying constraint factor (C^*) considering yield stress, Young's modulus and indentation strain is presented, using the ratio of the unloading and loading slope (μ) of the load/contact displacement curves. Matching the flow curves from uniaxial pillar compression and spherical indentation on NC Ni leads to an empiric relation $C^* = f(\mu)$ which is in accordance to previous FEM studies.

vi. Using the presented refinements leads to excellent agreement of flow curves obtained by uniaxial compression and spherical indentation for the tested materials NC Ni UFG Cu, UFG Cr and UFG W.

The presented advancements of spherical indentation testing and analysis will prospectively expand the possibilities of this technique. Apparently, a reasonable tip shape function and strain-rate controlled experiments contribute to a significantly improved utility of indentation tests. However, particularly the conversion from hardness to representative stress must be used with caution, as it could not yet be thoroughly physically explained. The application is restricted to materials with small internal length-scales and similar mechanical character to avoid tip size-effects and vastly different work hardening behavior. Besides, the properties of the tribological system of indenter tip and sample must be consistent. Consideration of these influences to extend the feasibility of the approach will be subject of future studies.

Acknowledgements

Appendix A

The conventional definition of strain from the classical Tabor approach and the novel definition of Kalidindi and Pathak are closely related. Both are dependent on the current opening angle θ (see Fig. A1).

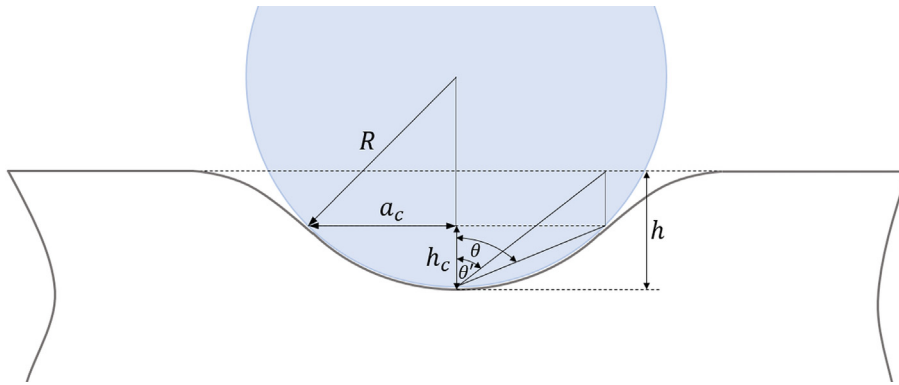| Tabor related definition	Definition by Kalidindi and Pathak
$\varepsilon_i = \frac{a_c}{R}$	$\varepsilon_i = \frac{4 \cdot h}{3 \cdot \pi \cdot a_c}$
$A_c = a_c{}^2 \cdot \pi$	$\frac{h}{a_c} = \cot\theta'$
$a_c = h_c \cdot \tan\theta$	$\frac{\cot\theta'}{\cot\theta} = \frac{h}{h_c}$
$R^2 = a_c{}^2 + (R - h_c)^2$	$\cot\theta' = \frac{h}{h_c} \cdot \cot\theta$
$R = \frac{a_c{}^2 + h_c{}^2}{2 \cdot h_c}$	$\varepsilon_i = \frac{4 \cdot h \cdot \cot\theta}{3 \cdot \pi \cdot h_c}$
$\frac{a_c}{R} = \frac{2 \cdot h_c \cdot a_c}{a_c{}^2 + h_c{}^2} = \frac{2 \cdot \cot\theta}{1 + \cot^2\theta}$	
$\varepsilon_i = f(\cot\theta)$	$\varepsilon_i = f(\cot\theta)$

Fig. A1. Schematic loading of a spherical tip with radius R.

Appendix B

The ratio of unloading slope, which is the contact stiffness S, and loading slope n_L, referred to as μ in this study, in indentation experiments is of interest to identify the character of plastic deformation, since it is directly related to the ratio of induced plastic and elastic work during indentation. The subsequent derivation shows that μ is in directly related to the elastic (E^*) and plastic (H) properties as well as to the indentation strain ε_i which scales with cot Θ (see Appendix A).

$$\mu = \frac{S}{n_L}$$

$$S = \frac{2 \cdot E \cdot \sqrt{A_c}}{\sqrt{\pi}} = 2 \cdot E^* \cdot h_c \cdot \tan\theta$$

$$P = H \cdot a_c{}^2 \cdot \pi = H \cdot h_c{}^2 \cdot \tan^2\theta \cdot \pi$$

$$n_L = \frac{dP}{dh_c} = 2 \cdot H \cdot h_c \cdot \tan^2\theta \cdot \pi$$

$$\mu = \frac{S}{n_L} = \frac{2 \cdot E^* \cdot h_c \cdot \tan\theta}{2 \cdot H \cdot h_c \cdot \tan^2\theta \cdot \pi} = \frac{E^*}{H} \cdot \frac{\cot\theta}{\pi}$$

Due to elemental elastic contact mechanics based on Hertz, the contact depth h_c and elastic sink-in depth h_s are related to each other by:

$$h_c = h_s = \frac{1}{2} \cdot h$$

During elastic deformation, the unloading slope is equivalent to the loading slope, hence the slope of the contact loading is 0.5. Experiments with a 50 μm radius tip on fused quartz, where no plastic deformation is expected, demonstrates this behavior (Fig. B1a). On GaAs, one notes that until the pop-in event there is only elastic deformation, showing μ on a level of 0.5, which instantaneously increases after the pop-in (Fig. B1b). For Al, tested with a 5 μm tip, plasticity is observable immediately (Fig. B1c). Contrarily, for sharp self-similar tips and isotropic materials, μ shows a horizontal profile over displacement as H, E^* and cot Θ will remain constant in the self-similar indentation process. Varying the opening angle will shift the profiles in parallel (Fig. B1d).
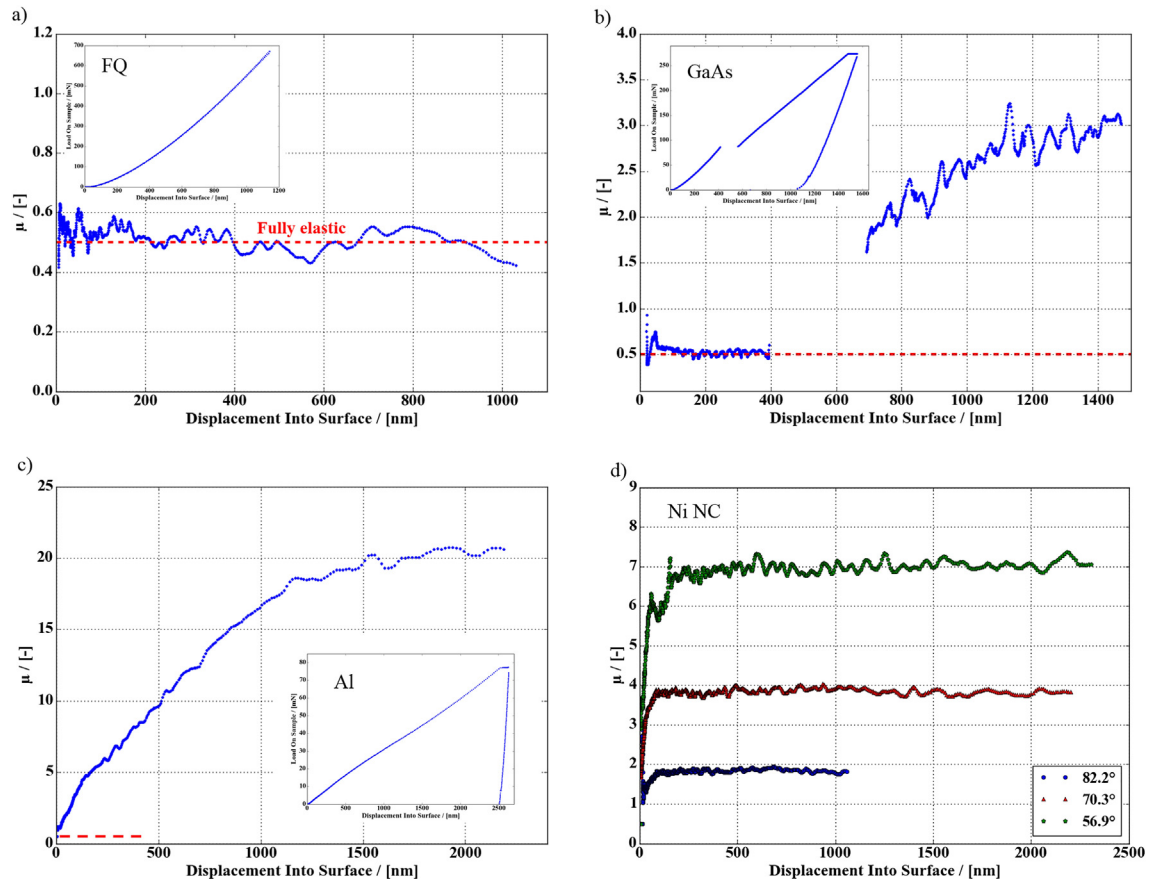
Fig. B1. Profile of μ over displacement. a) For a purely elastic indent on FQ with a 60 μm sphere μ is horizontal at a level of 0.5. Loading and unloading curve in the inset coincide. b) GaAs clearly demonstrates the transition from elastic to plastic deformation after the pop-in event. c) A spherical indent on Al shows plasticity instantaneously. d) μ is constant over displacement for self-similar pyramidal tips. A variation of the opening angle leads to a shift of the value of μ.

References

[1] J.B. Pethica, R. Hutchings, W.C. Oliver, Hardness measurement at penetration depths as small as 20 nm, Philos. Mag. A 48 (1983) 593–606, https://doi.org/10.1080/01418618308234914.

[2] W.C. Oliver, G.M. Pharr, An improved technique for determining hardness and elastic modulus using load and displacement sensing indentation experiments, J. Mater. Res. 7 (1992) 1564–1583, https://doi.org/10.1557/JMR.1992.1564.

[3] N.A. Stilwell, D. Tabor, Elastic recovery of conical indentations, Proc. Phys. Soc. 78 (1961) 169–179, https://doi.org/10.1088/0370-1328/78/2/302.

[4] I. Sneddon, The relation between load and penetration in the axisymmetric Boussinesq problem for a punch of arbitrary profile, Int. J. Eng. Sci. 3 (1965) 47–57, https://doi.org/10.1016/0020-7225(65)90019-4.

[5] J.L. Loubet, J.M. Georges, O. Marchesini, G. Meille, Vickers indentation curves of magnesium oxide (MgO), J. Tribol. 106 (1984) 43–48, https://doi.org/10.1115/1.3260865.

[6] M.F. Doerner, W.D. Nix, A method for interpreting the data from depth-sensing indentation instruments, J. Mater. Res. 1 (1986) 601–609, https://doi.org/10.1557/JMR.1986.0601.

[7] A.C. Fischer-Cripps, Nanoindentation, Springer, New York, 2002https://doi.org/10.1007/978-1-4419-9872-9.

[8] J.B. Pethica, W.C. Oliver, Mechanical properties of nanometre volumes of material: use of the elastic response of small area indentations, MRS Proc. 130 (1988) 13–23, https://doi.org/10.1557/PROC-130-13.

[9] S.A.S. Asif, K.J. Wahl, R.J. Colton, Nanoindentation and contact stiffness measurement using force modulation with a capacitive load-displacement transducer, Rev. Sci. Instrum. 70 (1999) 2408–2413, https://doi.org/10.1063/1.1149769.

[10] X. Li, B. Bhushan, A review of nanoindentation continuous stiffness measurement technique and its applications, Mater. Charact. 48 (2002) 11–36, https://doi.org/10.1016/S1044-5803(02)00192-4.

[11] W.C. Oliver, G.M. Pharr, Measurement of hardness and elastic modulus by instrumented indentation: advances in understanding and refinements to methodology, J. Mater. Res. 19 (2004) 3–20, https://doi.org/10.1557/jmr.2004.19.1.3.

[12] V. Maier, B. Merle, M. Göken, K. Durst, An improved long-term nanoindentation creep testing approach for studying the local deformation processes in nanocrystalline metals at room and elevated temperatures, J. Mater. Res. 28 (2013) 1177–1188, https://doi.org/10.1557/jmr.2013.39.

[13] K.L. Johnson, The correlation of indentation experiments, J. Mech. Phys. Solids. 18 (1970) 115–126, https://doi.org/10.1016/0022-5096(70)90029-3.

[14] W.D. Nix, H. Gao, Indentation size effects in crystalline materials: a law for strain gradient plasticity, J. Mech. Phys. Solids. 46 (1998) 411–425, https://doi.org/10.1016/S0022-5096(97)00086-0.

[15] G.M. Pharr, J.H. Strader, W.C. Oliver, Critical issues in making small-depth mechanical property measurements by nanoindentation with continuous stiffness measurement, J. Mater. Res. 24 (2009) 653–666, https://doi.org/10.1557/jmr.2009.0096.

[16] S. Qu, Y. Huang, G.M. Pharr, The indentation size effect in the spherical indentation of iridium: a study via the conventional theory of mechanism-based strain gradient plasticity, Int. J. Plast. 22 (2006) 1265–1286, https://doi.org/10.1016/j.ijplas.2005.07.008.

[17] K. Durst, M. Göken, G.M. Pharr, Indentation size effect in spherical and pyramidal indentations, J. Phys. D. Appl. Phys. 41 (2008) 1–5, https://doi.org/10.1088/0022-3727/41/7/074005.

[18] J.G. Swadener, E.P. George, G.M. Pharr, The correlation of the indentation size effect measured with indenters of various shapes, J. Mech. Phys. Solids. 50 (2002) 681–694, https://doi.org/10.1016/S0022-5096(01)00103-X.

[19] L. Prandtl, Über die Härte plastischer Körper, Nachrichten von Der Gesellschaft Der Wissenschaften Zu Göttingen. (1920) 74–85, https://doi.org/10.1007/978-3-662-11836-8_7.

[20] A.G. Atkins, D. Tabor, Plastic indentation in metals with cones, J. Mech. Phys. Solids. 13 (1965) 149–164, https://doi.org/10.1016/0022-5096(65)90018-9.

[21] D. Tabor, The Hardness of Metals, OUP, Oxford, 1951.

[22] J.L. Bucaille, S. Stauss, E. Felder, J. Michler, Determination of plastic properties of metals by instrumented indentation using different sharp indenters, Acta Mater. 51 (2003) 1663–1678, https://doi.org/10.1016/S1359-6454(02)00568-2.

[23] S. Shim, J. Jang, G.M. Pharr, Extraction of flow properties of single-crystal silicon carbide by nanoindentation and finite-element simulation, Acta Mater. 56 (2008) 3824–3832, https://doi.org/10.1016/j.actamat.2008.04.013.

[24] A. Leitner, V. Maier-Kiener, D. Kiener, Extraction of flow behavior and hall–Petch parameters using a nanoindentation multiple sharp tip approach, Adv. Eng. Mater. 19 (2017) 1–9, https://doi.org/10.1002/adem.201600669.

[25] Y.-T. Cheng, C.-M. Cheng, Can stress-strain relationships be obtained from indentation curves using conical and pyramidal indenters? J. Mater. Res. 14 (1999) 3493–3496, https://doi.org/10.1557/JMR.1999.0472.

[26] J.S. Field, M.V. Swain, A simple predictive model for spherical indentation, J. Mater. Res. 8 (1993) 297–306, https://doi.org/10.1557/JMR.1993.0297.

[27] M.D. Uchic, D.M. Dimiduk, J.N. Florando, W.D. Nix, Sample dimensions influence strength and crystal plasticity, Science 80 (305) (2004) 986–989, https://doi.org/10.1126/science.1098993.

[28] S. Basu, A. Moseson, M.W. Barsoum, On the determination of spherical nanoindentation stress-strain curves, J. Mater. Res. 21 (2006) 2628–2637, https://doi.org/10.1557/jmr.2006.0324.

[29] S.R. Kalidindi, S. Pathak, Determination of the effective zero-point and the extraction of spherical nanoindentation stress – strain curves, Acta Mater. 56 (2008) 3523–3532, https://doi.org/10.1016/j.actamat.2008.03.036.

[30] S. Pathak, J. Shaffer, S.R. Kalidindi, Determination of an effective zero-point and extraction of indentation stress – strain curves without the continuous stiffness measurement signal, Scr. Mater. 60 (2009) 439–442, https://doi.org/10.1016/j.scriptamat.2008.11.028.

[31] S. Pathak, S.R. Kalidindi, Spherical nanoindentation stress-strain curves, Mater. Sci. Eng. R. Rep. 91 (2015) 1–36, https://doi.org/10.1016/j.mser.2015.02.001.

[32] S.-D. Mesarovic, N.A. Fleck, Spherical indentation of elastic-plastic solids, Proc. R. Soc. London A Math. Phys. Eng. Sci. 455 (1999) 2707–2728, https://doi.org/10.1098/rspa.1999.0423.

[33] A.J. Bushby, N.M. Jennett, Determining the area function of spherical indenters for Nanoindentation, Mater. Res. Soc. Symp. Proc. 649 (2000) 1–6, https://doi.org/10.1557/PROC-649-Q7.17.

[34] A.J. Bushby, Nanoindentation using spherical indenters, Nondestruct. Test. Eval. 17 (2001) 213–234, https://doi.org/10.1080/10589750108953112.

[35] L. Hong, N. Fujisawa, M.V. Swain, Elastic modulus and stress – strain response of human enamel by nano-indentation, Biomaterials 27 (2006) 4388–4398, https://doi.org/10.1016/j.biomaterials.2006.03.045.

[36] D.K. Patel, S.R. Kalidindi, Correlation of spherical nanoindentation stress-strain curves to simple compression stress-strain curves for elastic-plastic isotropic materials using finite element models, Acta Mater. 112 (2016) 295–302, https://doi.org/10.1016/j.actamat.2016.04.034.

[37] P. Feldner, B. Merle, M. Göken, Determination of the strain-rate sensitivity of ultrafine-grained materials by spherical nanoindentation, J. Mater. Res. 49 (2017) 1466–1473, https://doi.org/10.1557/jmr.2017.69.

[38] B.-W. Choi, D.-H. Seo, J.-Y. Yoo, J. Jang, Predicting macroscopic plastic flow of high-performance, dual-phase steel through spherical nanoindentation on each micro-phase, J. Mater. Res. 24 (2009) 816–822, https://doi.org/10.1557/jmr.2009.0109.

[39] E. Meyer, Untersuchungen über Härteprüfung und Härte, Zeitschrift Verein Dtsch. Ingenieure (1909) 52.

[40] Y. Tirupataiah, G. Sundararajan, On the Constraint Factor Associated with the Indentation of Work-Hardening Materials with a Spherical Ball, Metall. Trans. A. 22A (1991) 2375–2384, https://doi.org/10.1007/BF02665003.

[41] J.L. Hay, W.C. Oliver, A. Bolshakov, G.M. Pharr, Using the ratio of loading slope and elastic stiffness to predict pile-up and constraint factor during indentation, MRS Proc. 522 (1998) 101–106, https://doi.org/10.1557/PROC-522-101.

[42] X. Chen, J.J. Vlassak, Numerical study on the measurement of thin film mechanical properties by means of nanoindentation, J. Mater. Res. 16 (2001) 2974–2982, https://doi.org/10.1557/JMR.2001.0408.

[43] A. Clausner, F. Richter, Determination of yield stress from nano-indentation experiments, Eur. J. Mech. A. Solids 51 (2015) 11–20, https://doi.org/10.1016/j.euromechsol.2014.11.008.

[44] M. Mata, O. Casals, J. Alcalá, The plastic zone size in indentation experiments: the analogy with the expansion of a spherical cavity, Int. J. Solids Struct. 43 (2006) 5994–6013, https://doi.org/10.1016/j.ijsolstr.2005.07.002.

[45] M. Rodríguez, J.M. Molina-Aldareguia, C. González, J. Llorca, Determination of the mechanical properties of amorphous materials through instrumented nanoindentation, Acta Mater. 60 (2012) 3953–3964, https://doi.org/10.1016/j.actamat.2012.03.027.

[46] S. Kang, Y. Kim, K. Kim, J. Kim, D. Kwon, Extended expanding cavity model for measurement of flow properties using instrumented spherical indentation, Int. J. Plast. 49 (2013) 1–15, https://doi.org/10.1016/j.ijplas.2013.02.014.

[47] B. Merle, V. Maier-Kiener, G.M. Pharr, Influence of modulus-to-hardness ratio and harmonic parameters on continuous stiffness measurement during nanoindentation, Acta Mater. 134 (2017) 167–176, https://doi.org/10.1016/j.actamat.2017.05.036.

[48] A. Leitner, V. Maier-Kiener, D. Kiener, Dynamic nanoindentation testing: is there an influence on a material's hardness? Mater. Res. Lett. 5 (2017) 486–493, https://doi.org/10.1080/21663831.2017.1331384.

[49] V. Maier, K. Durst, J. Mueller, B. Backes, H.W. Höppel, M. Göken, Nanoindentation strain-rate jump tests for determining the local strain-rate sensitivity in nanocrystalline Ni and ultrafine-grained Al, J. Mater. Res. 26 (2011) 1421–1430, https://doi.org/10.1557/jmr.2011.156.

[50] R. Fritz, D. Wimler, A. Leitner, V. Maier-Kiener, D. Kiener, Dominating deformation mechanisms in ultrafine-grained chromium across length scales and temperatures, Acta Mater. 140C (2017) 176–187, https://doi.org/10.1016/j.actamat.2017.08.043.

[51] R. Fritz, A. Leitner, V. Maier-Kiener, R. Pippan, D. Kiener, Interface-dominated Strength Scaling Behaviour in Ultrafine-grained Tungsten Samples, Submitted, 2017.

[52] M.D. Uchic, D.M. Dimiduk, A methodology to investigate size scale effects in crystalline plasticity using uniaxial compression testing, Mater. Sci. Eng. A 400–401 (2005) 268–278, https://doi.org/10.1016/j.msea.2005.03.082.

[53] D. Jang, J.R. Greer, Size-induced weakening and grain boundary-assisted deformation in 60 nm grained Ni nanopillars, Scr. Mater. 64 (2011) 77–80, https://doi.org/10.1016/j.scriptamat.2010.09.010.

[54] M.W. Kapp, A. Hohenwarter, S. Wurster, B. Yang, R. Pippan, Anisotropic deformation characteristics of an ultrafine- and nanolamellar pearlitic steel, Acta Mater. 106 (2016) 239–248, https://doi.org/10.1016/j.actamat.2015.12.037.

[55] R. Fritz, V. Maier-Kiener, D. Lutz, D. Kiener, Interplay between sample size and grain size: single crystalline vs. ultrafine-grained chromium micropillars, Mater. Sci. Eng. A 674 (2016) 626–633, https://doi.org/10.1016/j.msea.2016.08.015.

[56] T. Hausöl, H.W. Höppel, M. Göken, Tailoring materials properties of UFG aluminium alloys by accumulative roll bonded sandwich-like sheets, J. Mater. Sci. 45 (2010) 4733–4738, https://doi.org/10.1007/s10853-010-4678-y.

[57] H.S. Leipner, D. Lorenz, A. Zeckzer, H. Lei, P. Grau, Nanoindentation pop-in effect in semiconductors, Phys. B Condens. Matter 308–310 (2001) 446–449, https://doi.org/10.1016/S0921-4526(01)00718-9.

[58] S.A.S. Asif, J.B. Pethica, Nanoindentation creep of single-crystal tungsten and gallium arsenide, Philos. Mag. A 76 (1997) 1105–1118, https://doi.org/10.1080/01418619708214217.

[59] E.O. Hall, The deformation and ageing of mild steel: discussion of results, Proc. Phys. Soc. Sect. B. 64 (1951) 747, https://doi.org/10.1088/0370-1301/64/9/303.

[60] N.J. Petch, The cleavage strength of polycrystals, J. Iron Steel Inst. 174 (1953) 25–28.

[61] X. Li, K. Lu, Playing with defects in metals, Nat. Mater. 16 (2017) 700–701, https://doi.org/10.1038/nmat4929.

[62] L. Lu, X. Chen, X. Huang, K. Lu, Revealing the maximum strength in nanotwinned copper, Science 80 (323) (2009) 607–610, https://doi.org/10.1126/science.1167641.

[63] B. Merle, V. Maier, M. Göken, K. Durst, Experimental determination of the effective indenter shape and ε-factor for nanoindentation by continuously measuring the unloading stiffness, J. Mater. Res. 27 (2012) 214–221, https://doi.org/10.1557/jmr.2011.245.

[64] D.W. Marquardt, An algorithm for least-squares estimation of nonlinear parameters, J. Soc. Ind. Appl. Math. 11 (1963) 431–441, https://doi.org/10.1137/0111030.

[65] K. Levenberg, A method for the solution of certain non-linear problems in least squares, Q. Appl. Math. 2 (1944) 164–168, https://doi.org/10.1090/qam/10666.

[66] H. Hertz, Über die Berührung fester elastischer Körper, J. Für Die Reine Und Angew. Math. 92 (1882) 156–171, https://doi.org/10.1515/crll.1882.92.156.

[67] H. Majjad, S. Basrour, P. Delobelle, M. Schmidt, Dynamic determination of Young's modulus of electroplated nickel used in LIGA technique, Sensors Actuators A Phys. 74 (1999) 148–151, https://doi.org/10.1016/S0924-4247(98)00306-9.

[68] H.E. Boyer, T.L. Gall (Eds.), Metals Handbook, American Society for Metals, 1985.

[69] B.N. Lucas, W.C. Oliver, Indentation power-law creep of high-purity indium, Metall. Mater. Trans. A 30 (1999) 601–610, https://doi.org/10.1007/s11661-999-0051-7.

[70] G.M. Pharr, E.G. Herbert, Y. Gao, The indentation size effect: a critical examination of experimental observations and mechanistic interpretations, Annu. Rev. Mater. Res. 40 (2010) 271–292, https://doi.org/10.1146/annurev-matsci-070909-104456.

[71] E.W. Hart, Theory of the tensile test, Acta Metall. 15 (1967) 351–355, https://doi.org/10.1016/0001-6160(67)90211-8.

[72] Q. Wei, S. Cheng, K.T. Ramesh, E. Ma, Effect of nanocrystalline and ultrafine grain sizes on the strain rate sensitivity and activation volume: fcc versus bcc metals, Mater. Sci. Eng. A 381 (2004) 71–79, https://doi.org/10.1016/j.msea.2004.03.064.

[73] ISO, TR 29381 Metallic Materials - Measurement of Mechanical Properties by an Instrumented Indentation Test - Indentation Tensile Properties, 2008.

[74] Y.J. Park, G.M. Pharr, Nanoindentation with spherical indenters: finite element studies of deformation in the elastic – plastic transition regime, Thin Solid Films 448 (2004) 246–250, https://doi.org/10.1016/S0040-6090.